Mechanochemical synthesis of $Sn_{1-x}Mo_xO_2$ anode materials for Li-ion batteries

M. Martos, J. Morales and L. Sánchez*

Departamento de Química Inorgánica, Facultad de Ciencias, Universidad de Córdoba, Campus de Rabanales, Edificio C-3, 14071 Córdoba, Spain. E-mail: iq2sagrl@uco.es

$Sn_{1-x}Mo_xO_2$ mixed oxides of low crystallinity have been synthesized by mechanical milling of the starting elements in an air atmosphere at room temperature and investigated as electrode materials for lithium batteries. The oxides were characterized by X-ray diffraction, infrared spectroscopy and X-ray photoelectron spectroscopy. The results suggest that the Mo-doped samples are solid solutions with a cassiterite-type structure and Mo in the tetravalent oxidation state. Significant amounts of amorphous silica over the range 12–23% by weight as determined by energy dispersive analysis (EDX), and originating from the agate jar and balls of milling apparatus used for the experiments, were also detected. The compounds were tested as electrodes in secondary lithium batteries. The addition of Mo has two favourable effects, namely: (i) it increases the discharge capacity; and (ii) it improves capacity retention in cells cycled between 1.0 and 0.0 V. The formation of a Li–Mo–O oxide conductive matrix during the electrochemical insertion of lithium may account for this enhanced performance. In this reasoning, the silica present in the samples was assumed to play a minor role based on the stability of the Si–O bond.

Introduction

A new generation of lithium-ion batteries, the anodes of which are composed of tin-based compounds, was developed by FujiPhoto Film Celltec in early 1997.[1] Tin-based compounds are attractive on account of their high specific capacities and energy densities relative to carbon, the material commonly used as the anode in the manufacture of Li-ion cells. The large specific capacities exhibited by these tin-based systems are related to their ability to accommodate large amounts of lithium. The reaction with lithium is well known and involves a decomposition reaction that yields Li_2O and Sn, followed by the formation of various Li–Sn alloys.[2–4] The discharged electrode can be considered a composite system in which a Li_2O matrix binds Li–Sn regions and partly mitigates the large volume changes associated with alloying and de-alloying in reversible charge and discharge reactions.

Unfortunately, the use of tin-based oxide anodes has some drawbacks including: (i) a large irreversible capacity loss during the formation of lithium oxide in the first cell charge, a feature that raises manufacturing problems; (ii) the presence of inactive materials such as Li_2O in the rechargeable electrochemical process, which depresses the energy density; (iii) the critical role of metal particle size, which affects the cycle life; and (iv) volume and voltage changes, which may compromise safety.

Special endeavours have been devoted to deciphering the role played by the presence of an inert or active glue matrix in the anode material, which helps mitigate disintegration and mechanical failure of the electrode through the significant volume changes undergone by the tin particles as Li_xSn alloys are formed. In this context, good results have been obtained by using amorphous tin oxide glass composites (*e.g.* SnO_2–B_2O_3–P_2O_5)[5–8] and tin intermetallic compounds (*e.g.* Sn–Fe,[9] Cu–Sn,[10] Sn–Sb,[11] Ni–Sn,[12] Sn–Ca[13]), where the elements accompanying tin play the same role as Li_2O in the oxide materials. Occasionally, the preparation of these compounds requires high temperatures ($> 900\ °C$) and/or the use of an inert atmosphere. On the other hand, Sn–B–P–O composites exhibit a large irreversible capacity and a low volumetric capacity relative to tin oxides SnO and SnO_2.

One plausible alternative involves doping tin oxides with elements that improve their electrochemical performance as a result of the presence of a new inert matrix together with Li_2O. By controlling the doping agent, one can preserve the reversible capacity while improving the cycling behaviour of SnO_2 anodes. Doped systems such as $Sn_xSi_yO_2$,[14] $Sn_xB_yO_2$[15] and even mixtures such as SnO_2–C[16] and SnO–ZnO[17] have been tested for this purpose.

In previous papers, we reported on the favourable effects of the presence of Mo in a SnO_2 matrix[18,19] towards its reaction with lithium. Molybdenum-doped samples were prepared by low-temperature aqueous methods and the presence of Mo was found to alter the habit growth of SnO_2 crystals, to increase lithium mobility and have a diluting effect. These effects account for the improved electrochemical performance observed. One of the main difficulties encountered in these arose from the need to control the Mo : Sn ratio, which has significant effects on electrochemical properties. Aqueous methods exposed an appreciable difference between the starting and final Sn : Mo ratio, the origin of which might be incomplete precipitation of Sn and/or Mo ions. An alternative, simple way of overcoming this drawback is by using mechanochemical methods of synthesis. These methods have gained interest in the field of Li-ion batteries[20,21] on account of improved electrochemical properties of the materials they provide. This paper reports a mechanochemical procedure for preparing Mo-doped SnO_2 from Sn–Mo mixtures of known compositions as well as a study of their electrochemical properties in lithium cells.

Experimental

The starting materials were normally stoichiometric mixtures of elemental powders of Sn (Aldrich Chemical, 99.5% pure) and Mo (Merck Chemical, 99.9% pure). Mixtures were milled in a Retsch ball mill where both the pot and the balls were made of agate. The volume of the pot and the number of 20 mm diameter balls were 200 mL and 5, respectively. All grinding

tests were carried out by starting from 1 g of sample. Ball milling was done in the air at 60 rpm for one week.

The final stoichiometry was confirmed by repeated electron microprobe dispersive X-ray analyses (EDX) performed on Jeol JMS 6400 microscope. X-Ray diffraction (XRD) patterns were obtained on a Siemens D5000 X-ray diffractometer using CuKα radiation and a graphite monochromator, in steps of 0.02° and 1.2 s. X-Ray photoelectron spectra (XPS) were recorded on a Physical Electronics PHI 5700 spectrometer using non-monochromated MgKα radiation and a hemispherical analyser operating in the constant pass mode at 29.35 eV. Binding energies (BE) were referred to the C 1s peak at 284.8 eV. Samples were mounted on a holder without adhesive tape and kept under high vacuum in the preparation chamber overnight before they were transferred to the analysis chamber of the spectrometer. Survey spectra over the range 0–1200 eV were recorded at a 187.85 pass energy, each region being scanned several times to ensure an adequate signal-to-noise ratio. IR spectra were obtained on a FTIR Perkin Elmer Spectrum 2000 instrument, using powder samples that were ground and pressed into KBr pellets. Thermogravimetric (TG) measurements were made on a Cahn 2000 thermobalance by heating from 25 to 800 °C at a rate of 2.5 °C min^{-1} under ambient conditions.

Electrochemical experiments were carried out in two-electrode cells, using lithium as anode. The electrolyte was 1 M anhydrous $LiPF_6$ in a 1 : 1 mixture of ethylene carbonate (EC) and dimethyl carbonate (DMC). Oxide electrode pellets (7 mm diameter) were prepared by pressing, in a stainless steel grid, ca. 4 mg of active material with polytetrafluoroethylene (PTFE) [5 wt% (w/o)], and acetylene black (10 w/o) at 4 tons. Lithium foil was cut into circles 7 mm in diameter. Unless otherwise noted, cells were cycled at a 0.25 mA cm^{-1} current density controlled via a MacPile II Potentiostat-galvanostat.

Results and discussion

Structural characterization

As can be inferred from the XRD patterns of Fig. 1, all samples consisted of a single phase with a cassiterite-like structure,
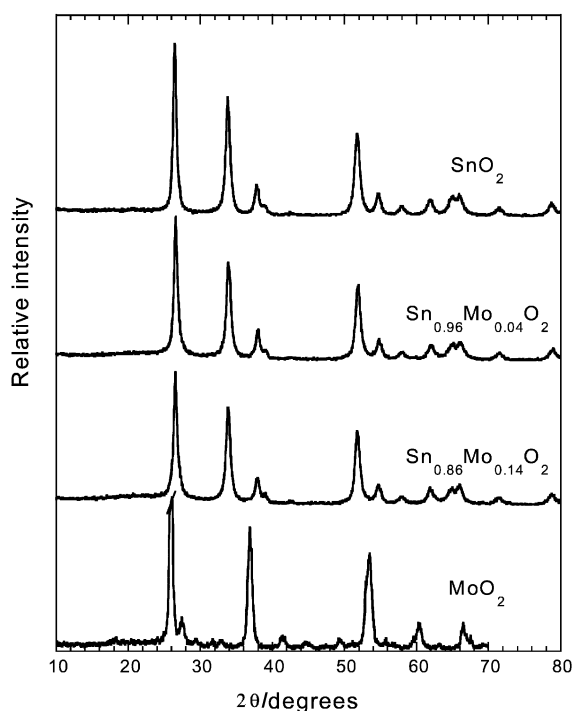
Table 1 Unit cell parameters and crystallite size of SnO_2 and $Sn_{1-x}Mo_xO_2$ samples

Sample	a/Å	c/Å	L_{110}/Å	L_{101}/Å	V/Å^3
SnO_2	4.736(1)	3.182(1)	208	169	71.37
$Sn_{0.96}Mo_{0.04}O_2$	4.728(3)	3.176(3)	206	166	70.99
$Sn_{0.86}Mo_{0.14}O_2$	4.740(4)	3.178(4)	224	171	71.40

SnO_2. No additional lines belonging to other phases of Sn or Mo, such as SnO or MoO_3, were detected. Only when milling was stopped after 24 or 72 h was elemental tin or molybdenum detected as an impurity. The mechanochemical process can therefore induce the oxidation of Sn and Mo, leading to the subsequent formation of a SnO_2-based phase. Also, the cassiterite structure remains unaltered in the presence of even large amounts of doping molybdenum. The values of the cell parameters are shown in Table 1. The cell volume is similar for the three samples and no clear-cut correlation between the a or c values and the Mo content is apparent. Nevertheless, when pure Mo is subjected to a similar treatment, the element is oxidized to MoO_2 [see Fig. 1 (bottom spectrum)]. Molybdenum seems to have no significant influence on the habit growth of the crystals either. Thus, the intensity of the diffraction peaks (Fig. 1) and the crystallite size of the particles, calculated by applying the Scherrer equation[22] to the two main reflections and collected in Table 1, change little with the Mo content. The TG measurements confirm the absence of water in the structure.

There are significant differences in morphological properties between Sn–Mo powders prepared by mechanochemical synthesis and those obtained via a precipitation reaction.[19] Thus, the presence of Mo in the latter decreases cell volume and enhances crystallite growth along the [hk0] direction. Also, wet chemical procedures yield powders of poorer crystallinity as particles exhibit crystallite sizes three times lower than those shown in Table 1. On the other hand, mechanochemical synthesis has two main advantages, namely: (i) better control of the mixed oxide stoichiometry, and (ii) the resulting powders are anhydrous.

Indirect evidence of the presence of molybdenum ions in the cassiterite-like structure was obtained by interpretating the IR and XPS data. Fig. 2 shows the IR spectra. The broad band below 700 cm^{-1}, with peaks at 670, 615 and 553 cm^{-1}, for undoped SnO_2 was assigned to different vibration modes of O–Sn–O and Sn–O–Sn groups.[23] The presence of a broad band centred at 1100 cm^{-1} and of two peaks at 807 and 483 cm^{-1} is an unexpected feature of the SnO_2 IR spectrum and must be associated with the presence of amorphous SiO_2.[24] This phase is not apparent from the XRD measurements and results from wear of the agate pot and balls during the grinding process. According to the literature,[25,26] the band at 1100 cm^{-1} is associated with the stretching vibration mode of the Si–O bond, whereas the bands at ca. 810 and 490 cm^{-1} correspond to the bending modes of the Si–O–Si group. Based on similar IR results, Huang et al.[24] suggested the formation of $Sn_{1-x}Si_xO_2$ solid solutions from $SnCl_4$ and $Si(OEt)_4$ solutions which were pyrolysed at temperatures above 800 °C. We believe that the IR data provide too weak evidence to check this hypothesis, taking into account the difficulty of having Si in octahedral coordination.

Although the IR spectra for the Sn–Mo system exhibit the above-described main features, some special characteristics are worth mentioning. Thus, two new bands at 947 and 800 cm^{-1}, the intensities of which increase with increasing Mo content, account for the presence of Mo and are assigned to Mo–O stretching modes. Based on the assignations of Krasovec et al.,[23] the more prominent band at 947 cm^{-1} can be ascribed to stretching modes of the terminal Mo–O bond (with a certain amount of double bond character). If we assume that
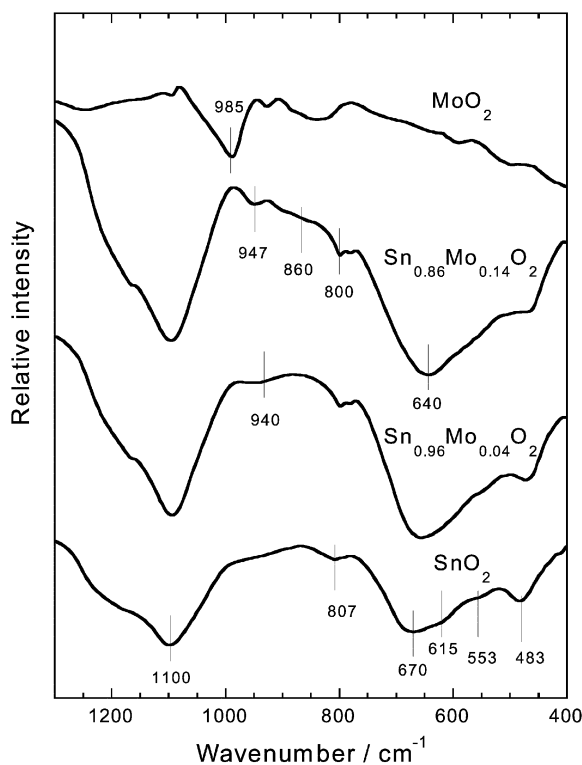

Fig. 1 XRD patterns for SnO_2, $Sn_{1-x}Mo_xO_2$ and MoO_2 samples obtained by grinding.

Fig. 2 IR transmission spectra for SnO_2, $Sn_{1-x}Mo_xO_2$ and MoO_2 samples obtained by grinding.

molybdenum ions occupy octahedral positions in a random distribution in the cassiterite-like structure, the 800 cm^{-1} band, and the low intensity band at 860 cm^{-1} for the $Sn_{0.86}Mo_{0.14}O_2$ sample, most likely correspond to the bridging Mo–O–Mo and Sn–O–Mo modes. The IR transmission spectra for Mo-containing SnO_2 also provide evidence about the variation of the local environment of SnO_2 after Mo-doping. The split band around 670 cm^{-1} shifts to 640 cm^{-1} and that at *ca.* 555 cm^{-1} disappears as the Mo content increases. Both bands are related to the Sn–O stretching mode of SnO_2.

The IR spectrum for pure ground Mo, clarifies some points concerning the Mo state in the Mo-containing SnO_2 samples. In these samples, the strong band at 985 cm^{-1}, present in the

Mo ground sample and assigned to the symmetric stretching vibration,[27] is absent. This seems to rule out the formation of MoO_2 as an independent phase and confirms that Mo is inseparable from the SnO_2 matrix, with which it forms a true solid solution. Moreover, the intensities of the peaks associated with silica impurities coming from the balls and the jar are significantly decreased. One plausible explanation is that Mo tends to form a protective layer on the balls and on the container surface.

The binding energy (BE) values for the core level of the elements in the different samples are shown in Table 2. The atomic ratios obtained from the peak areas as corrected with the sensitivity factors for the elements[28] are shown in Table 3. For comparison, the atomic ratios obtained with EDX are also listed. The 3d doublet for Sn is rather symmetric and the BE changes little with grinding conditions, the values being consistent with those reported for SnO_2,[28] Fig. 3a. All O 1s spectra for the three ground samples have two components, at 531 and 533 eV; the intensity of the latter decreases as the Mo content increases (see Fig. 3b). We can tentatively assign these
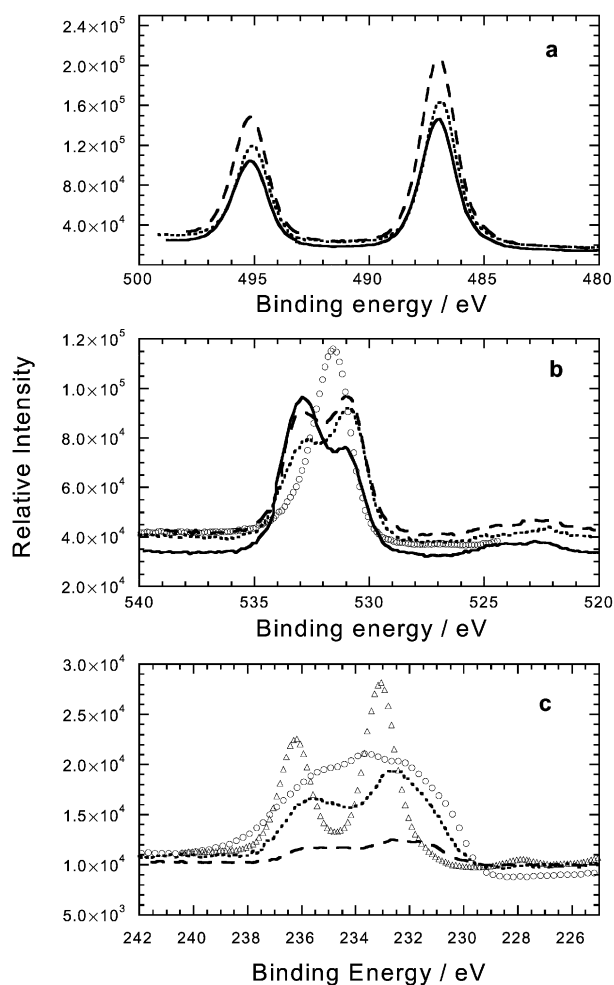

Fig. 3 (a) Sn 3d, (b) O 1s and (c) Mo 3d core level spectra for SnO_2 (—), $Sn_{0.96}Mo_{0.04}O_2$ (– –), $Sn_{0.86}Mo_{0.14}O_2$ (···), MoO_2 (○) and MoO_3 (△) samples.

Table 2 Binding energies, in eV, of the main core level spectra for Sn, Mo and Sn + Mo ground in air for one week. The spectrum for commercial MoO_3 is included for comparison

Sample	Sn 3d	Mo 3d	Si 2p	O 1s
Sn	487	—	103	531
	495			533
Sn + Mo (%Mo = 4)	487	232	103.5	531
	495	235		533
Sn + Mo (%Mo = 14)	487	232.5	103.5	531
	495	235.5		533
Mo	—	232.0	—	531.6
		235.3		
		233.7		
MoO_3	—	233	—	531
		236.2		

Table 3 Atomic ratios of ground samples as obtained by spectroscopic methods

Sample	Mo : Sn^a	Mo : Sn (EDX)	Si : Sn (EDX)	Mo : Sn (XPS)	Si : Sn (XPS)
Sn	—	—	0.74	—	—
Sn + Mo (%Mo = 4)	0.038	0.043	0.55	0.044 (0.040)	0.6 (0.42)
Sn + Mo (%Mo = 14)	0.218	0.16	0.42	0.23 (0.18)	0.52 (0.37)

^{a}Starting composition. Values in brackets were obtained after sputtering with Ar$^+$ for 2 min.

two signals to the two main components, namely the cassiterite-based particles and amorphous silica. The higher energy peak is assigned the silica impurities based on two features. First, the intensity of the Si 2p peak also decreases with increasing Mo content (see Table 3). Second, the O 1s spectrum for pure ground Mo exhibits a rather symmetric profile centred at 531.6 eV. These results are consistent with the above-described IR spectra as regards the tendency of Mo to reduce the silica content. Fig. 3c shows the Mo 3d core level spectra. In order to account for its oxidation state, it helps to compare these spectra with those for pure ground Mo – MoO_2 according with the X-ray data – and commercial MoO_3 (also included in the same figure). The following considerations can be made: like commercial MoO_3, the Mo-doped samples exhibit a simple, well-defined spin-orbit doublet, particularly at a high Mo content. This suggests, as expected for MoO_3, that metal atoms at the surface are predominantly in a single oxidation state. With Mo-doped samples, however, a shift in the Mo 3d peak by 1 eV to lower binding energies is observed. Such a shift to lower BE may reflect a lower oxidation state for Mo (probably as Mo^{4+}). A more complex profile was obtained for pure ground Mo. The core level spectrum is characterized by a broad, asymmetric band that consist of at least three overlapping peaks centred at 232.0, 233.7 and 235.3 eV, with shoulders at 230.4 and 236.5 eV. Based on the above considerations, we interpret this complexity by assuming the presence of different oxidation states, mainly Mo^{4+} and Mo^{6+}. The shoulder at the lower BE values might reflect the presence of unoxidized Mo. These results reveal that, in SnO_2, Mo participates as a tetravalent cation, probably replacing Sn^{4+} and forming a solid solution. The fact that the lattice dimensions undergo insignificant changes with the Mo content is consistent with the similarity between the ionic radii of Mo^{4+} (0.83 Å) and Sn^{4+} (0.79 Å). By contrast, the unit cell parameters for the doped samples obtained from precipitation methods have a slight tendency to decrease as the Mo content increases. The strong oxidizing conditions used account for the presence of Mo^{6+} in the cassiterite network, confirmed by XPS measurements.[29] The smaller ionic radius of Mo^{6+} (0.62 Å) compared with Sn^{4+} accounts for the unit cell contraction. Moreover, this substitution increases Mo^{4+} stability, in contrast with the MoO_2 particles obtained by grinding, the surface of which is partially oxidized. The peak shape found in this work differs from that reported by Gulino et al.[30] for a MoO_2 clean surface. These authors described the Mo 3d core level as a complex signal composed of a pair of overlapping doublets, the origin of which was ascribed to the metal–metal bond, which is important in this compound. The greater simplicity of our spectra (Fig. 3c) provides additional support for the substitution model and the Mo atom dispersion should prevent metal–metal bond formation.

The Mo:Sn ratios obtained with the two composition methods used, Table 3, are fairly consistent with the starting mixtures and account for a uniform distribution of Mo. The doped sample compositions calculated from triplicate EDX values were as follows: $Sn_{0.96}Mo_{0.04}O_2$, $Sn_{0.86}Mo_{0.14}O_2$ with a content in amorphous SiO_2 of 17.4 ± 0.2 and 12.7 ± 0.2%, respectively. For pure ground Sn an amount of 23.1 ± 0.7% of silica was derived. These percentages are referred to weight. However, somewhat different values were obtained from XPS measurements (see Table 3) owing to the differences in sample depth that these analytical techniques can examine.

Electrochemical properties

Fig. 4 shows the first galvanostatic discharges performed on Li/SnO_2 and $Li/Sn_{1-x}Mo_xO_2$ cells. Two main reactions account for the occurrence of the two *pseudo*-plateaux at 1.0 and 0.4 V in the discharge curve. The first involves the reduction of Sn^{4+} to Sn^0, which is accompanied by the formation of Li_2O. The
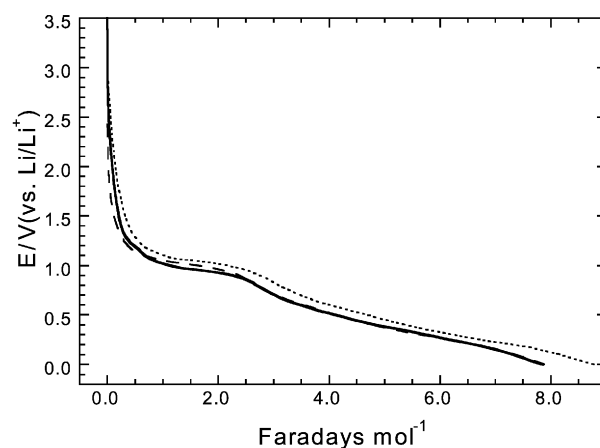

Fig. 4 First-discharge galvanostatic curves for Li/SnO_2 (—), (b) $Li/Sn_{0.96}Mo_{0.04}O_2$ (– – –) and (c) $Li/Sn_{0.86}Mo_{0.14}O_2$ (···) cells.

lower potential step must be related to the formation of Li_xSn alloys with $x = 4.4$–3.5. Doping with Mo introduces small differences in the discharge profiles (particularly, a slight decrease in electrode polarization). A similar behaviour was also observed in the first plateau of the samples prepared in an aqueous solution.[18,19] However, increasing the lithium content in these latter samples resulted in steeper voltage drops (and hence in smaller discharged depths) than with the undoped sample. Developing an accurate model for explaining such a subtle divergence is especially difficult owing to the many differences found between the results of the two synthetic procedures, namely: particle shape and microstructure, Mo oxidation state, hydration degree, impurities, etc., which can even act in opposite directions. In any case, the presence of Mo in the cassiterite-like structure enhances the ionic conductivity,[19] thereby increasing the potential of the discharge curve and allowing the formation of the $Li_{4.4}Sn$ alloy. For the $Sn_{0.86}Mo_{0.14}O_2$ electrode, the amount of lithium inserted exceeds that required to account for both reactions by more than 5%. The following arguments can help explain these results: (i) the amenability of Mo^{4+} ions to reduction to lower oxidation states;[31] and (ii) an irreversible process of electrolyte decomposition resulting in the formation of a passive layer on the surface of tin oxide particles.[32]

The reversibility of the electrochemical alloying/de-alloying process was studied in the light of differential capacity plots.[33] Fig. 5 shows the dq/mdV vs. potential plots for the first, fifth, tenth and twentieth charge–discharge sequences of Li/LPF_6-(EC-DMC)/SnO_2 and of Li/LPF_6(EC-DMC)/$Sn_{0.86}Mo_{0.14}O_2$ cells between 0.0 and 1.0 V. These potential–capacity curves correspond to the lower potential plateau where Li_xSn alloys are formed. The reversibility of the oxidation–reduction process is apparent from the symmetric anodic and cathodic waves obtained.

As previously reported,[19] the Li–Mo–O oxides act as spectators or inert matrices with regard to the alloy formation process. A similar role can be inferred from the differential specific capacity plots. The potential profiles for the $Sn_{1-x}Mo_xO_2$ compounds reveal a high similarity with SnO_2 and other tin-based anodes previously reported.[33] This suggests that the reaction mechanism for these doped electrodes is very similar to that for SnO_2 and that their electrochemical behaviour is essentially controlled by the reactions of lithium with tin atoms. The reduction profiles for undoped and low-doped samples (Fig. 5) exhibit two major components, *viz.* a strong peak at 0.25 V and the weak, ill-defined peak at 0.075 V. The latter corresponds to the formation of Li_xSn alloys of high Li content, the reversibility of which is unclear. Upon cycling, a fast decrease in wave intensity is observed in the Li/SnO_2 cell, together with the appearance of new shoulders
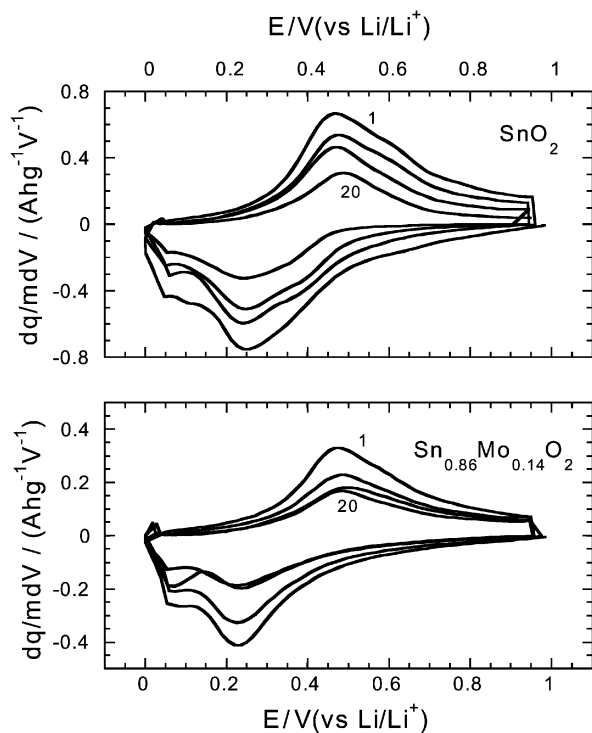
Fig. 5 Differential capacity plots for Li/SnO$_2$ and Li/Sn$_{0.86}$Mo$_{0.14}$O$_2$ cells.

at 0.4 and 0.6 V in the discharge and charge curves, respectively, which can be ascribed to the aggregation of tin or lithium–tin atoms into increasingly large clusters upon cycling.[3] Aggregation would cause fragmentation and the loss of contact between particles of the material, leading to an irreversible lithium insertion–extraction process. This phenomenon is lessened by the presence of the Li–Mo–O oxides, which form a conductive matrix that disperses the tin atoms towards the reaction with lithium. The preservation of the single peak at *ca.* 0.2 V upon successive cycling in the Li/Sn$_{0.86}$Mo$_{0.14}$O$_2$ cell may provide confirmation for the above assumptions.

In the electrochemical calculations, the silica present in the samples was assumed to remain unreacted because the strong Si–O bond cannot be broken by lithium.[14] In fact, no new signals were detected in the dq/mdV plots compared with pure SnO$_2$, which indicates that the electrochemical process is controlled by SnO$_2$-based particles.

The specific capacity delivered by the cells made from the studied samples, cycled between 0.0 and 1.0 V, is shown as a function of cycle number in Fig. 6a. As a rule, increased Mo contents resulted in improved capacity retention. However, highly doped samples delivered small specific capacities because the Mo atoms simply added weight to the electrode, acting as an inactive material in the electrochemical process. Moreover, the presence of Mo also increased the coulombic efficiency of the cells. Thus, a highest Li : Sn ratio can be reversibly extracted on cycling the doped samples (Fig. 6b), leading to an increase in charge recovery – a term that defines the specific capacity stored by the cell in the charge process in relation to that delivered in the previous discharge process – by increasing the Mo content (Fig. 6c), which helps to retain the specific capacity delivered. The beneficial effect of Mo on the electrochemical performance properties was also observed in Sn–Mo samples prepared by precipitation.[19] In this case, the capacity on cycling was somewhat higher (particularly in the 2% Mo samples). The crystallite sizes found in this series (three times lower than those for the ground samples) may account for their improved capacity. However, the difficulty of acquiring an accurate knowledge of the composition of the ground samples owing to the presence of amorphous silica – which may
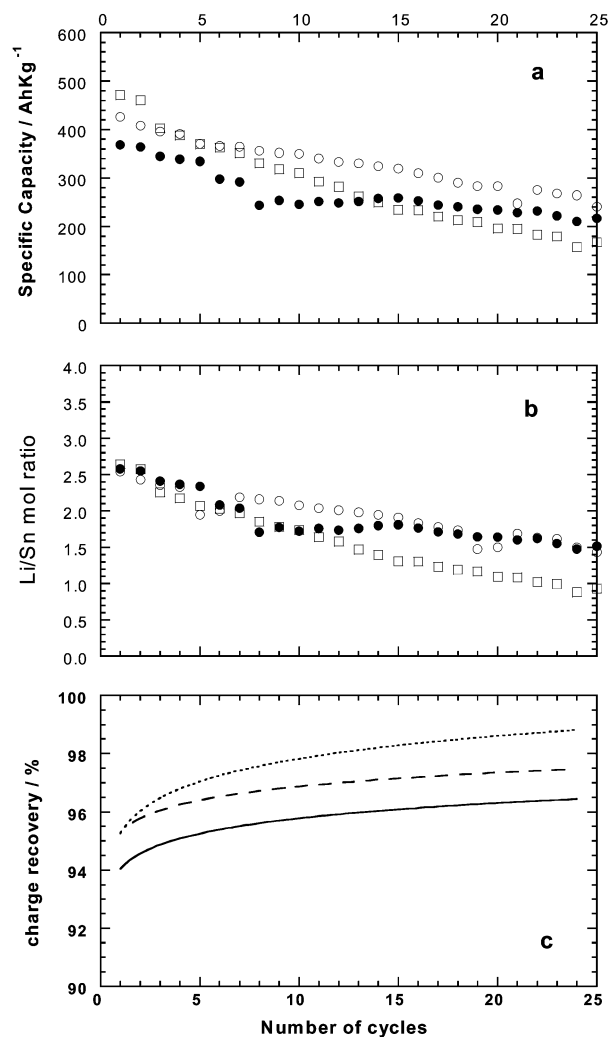

Fig. 6 Changes in (a) specific capacity, (b) extracted Li/Sn ratio and (c) charge recovery of Li/SnO$_2$ ($\square$ or —), Li/Sn$_{0.96}$Mo$_{0.04}$O$_2$ ($\bigcirc$ or $- - -$) and Li/Sn$_{0.86}$Mo$_{0.14}$O$_2$ ($\bullet$ or ⋯) cells on cycling.

affect the electrochemical calculations – must be the main disadvantage of this, otherwise, simple and fast synthetic route. However, the Sn–Mo samples obtained by mechanochemical synthesis exhibited a lower irreversible capacity because their water content was negligible.

Conclusions

The mechanochemical treatment of Sn, Mo and a mixture of both elements in air yields SnO$_2$, MoO$_2$ and Sn$_{1-x}$Mo$_x$O$_2$ solid solutions (x up to 0.14), respectively. The mixed oxides adopt a cassiterite-type structure with Mo^{4+} occupying octahedral positions in a random distribution but introducing little changes in the unit cell parameters compared with undoped SnO$_2$. Relative to wet chemical procedures, the mechanochemical synthesis allows better control of the mixed oxide stoichiometry and crystallite habit growth; also, the resulting powder is anhydrous. Although its influence on the active material towards lithium is insignificant, the presence of amorphous silica as impurities can pose some problem (mainly errors in assessing contents). These SnO$_2$-based materials were tested as electrodes in Li/SnO$_2$ and Li/Sn$_{1-x}$Mo$_x$O$_2$-type cells, especially over the 0.0–1.0 V range, where reversible Li$_x$Sn alloys are formed. The presence of Mo was found to improve cell performance, particularly as regards coulombic efficiency. Thus, charge recovery improved with an increase in the Mo

content. The diluent effect of Mo hindering the aggregation of tin or lithium–tin atoms in large clusters on cycling may account for its favourable effect. These properties make molybdenum-doped tin oxides attractive candidates to act as anodes for Li-ion batteries.

Acknowledgements

References

1   Y. Idota, M. Mishima, M. Miyaki, T. Kubota and T. Misayaka, *Eur. Pat. Appl*, 651450 A1 950503, 1997.
2   I. A. Courtney and J. R. Dahn, *J. Electrochem. Soc.*, 1997, **144**, 2045.
3   I. A. Courtney, W. R. McKinnon and J. R. Dahn, *J. Electrochem. Soc.*, 1999, **146**, 59.
4   I. A. Courtney, R. A. Dunlap and J. R. Dahn, *Electrochim. Acta*, 1999, **45**, 51.
5   Y. Idota, T. Kubota, A. Matsufuji, Y. Maekawa and T. Misayaka, *Science*, 1997, **276**, 1395.
6   H. Morimoto, M. Nakai, M. Tatsumisago and T. Minami, *J. Electrochem. Soc.*, 1999, **146**, 3970.
7   J. Y. Kim, D. E. King, P. N. Kumta and G. E. Blomgren, *J. Electrochem. Soc.*, 2000, **147**, 4411.
8   J. Y. Lee, Y. Xiao and Z. Liu, *Solid State Ionics*, 2000, **133**, 25.
9   O. Mao and J. R. Dahn, *J. Electrochem. Soc.*, 1999, **146**, 414.
10 K. D. Kepler, J. T. Vaughey and M. M. Thackeray, *Electrochem. Solid State Lett.*, 1999, **2**, 307.
11 J. Yang, Y. Takeda, N. Imanishi and O. Yamamoto, *J. Electrochem. Soc.*, 1999, **146**, 4009.
12 G. M. Ehrlich, C. Durand, X. Chen, T. A. Hugener, F. Spiess and S. L. Suib, *J. Electrochem. Soc.*, 2000, **147**, 886.
13 L. Fang and B. V. R. Chowdari, *J. Power Sources*, 2001, **97–98**, 181.
14 H. Huang, E. M. Kelder, L. Chen and J. Schoonman, *J. Power Sources*, 1999, **81–82**, 362.
15 J. Morales and L. Sánchez, *Solid State Ionics*, 1999, **3–4**, 219.
16 J. Read, D. Foster, J. Wolfenstine and W. Behl, *J. Power Sources*, 2001, **96**, 277.
17 F. Belliard and J. T. S. Irvine, *J. Power Sources*, 2001, **97–98**, 362.
18 J. Morales and L. Sánchez, *J. Electrochem. Soc.*, 1999, **146**, 1640.
19 M. Martos, J. Morales and L. Sánchez, *Electrochim. Acta*, 2000, **46**, 83.
20 H. Morimoto, M. Tatsumisago and T. Minami, *Electrochem. Solid State Lett.*, 2001, **4**, A16.
21 H. Kim, Y. J. Kim, D. G. Kim, H. J. Sohn and T. Kang, *Solid State Ionics*, 2001, **144**, 41.
22 H. P. Klug and L. E. Alexander, *X-Ray Diffraction Procedures for Polycrystalline and Amorphous Materials*, Wiley, New York, 1974, p. 665.
23 U. O. Krasovec, B. Orel, S. Hocevar and Y. Musevic, *J. Electrochem. Soc.*, 1997, **144**, 3398.
24 H. Huang, E. M. Kelder, L. Chen and J. Schoonman, *Solid State Ionics*, 1999, **120**, 205.
25 R. A. Nyquist and R. O. Kage, *Infrared Spectra of Inorganic Compounds*, Academic Press, New York, 1971.
26 J. A. Navio, M. Macias, G. Colón, P. J. Sánchez-Sota, V. Augugliaro and L. Palmisano, *Appl. Surf. Sci.*, 1994, **81**, 325.
27 M. Zhon and L. Andrews, *J. Chem. Phys.*, 1999, **111**, 4230.
28 J. F. Moulder, W. E. Stickle, P. E. Sobol and K. D. Bumber, in *Handbook of X-Ray Photoelectron Spectroscopy*, J. Chastain, ed., Perkin-Elmer Corporation, Physical Electronics Division, 1979.
29 M. Martos, Ph. D. Thesis, University of Córdoba, Spain, 2002.
30 A. Gulino, S. Parker, F. H. Jones and R. G. Edgell, *J. Chem. Soc., Fadaray Trans.*, 1996, **92**, 2137.
31 A. Manthiram and C. Tsang, *J. Electrochem. Soc.*, 1996, **143**, L143.
32 H. Li, X. Huang and L. Chen, *Electrochem. Solid State Lett.*, 1998, **1**, 241.
33 I. A. Courtney and J. R. Dahn, *J. Electrochem. Soc.*, 1997, **144**, 2943.